Environmental Pollution 265 (2020) 115079

Contents lists available at ScienceDirect

Environmental Pollution

journal homepage: www.elsevier.com/locate/envpol

The driving factors of mercury storage in the Tibetan grassland soils underlain by permafrost☆

Jing Gu [a], Qiaotong Pang [a], Jinzhi Ding [b], Runsheng Yin [c], Yuanhe Yang [d], Yanxu Zhang [a, *]

[a] School of Atmospheric Sciences, Nanjing University, Nanjing, 210023, China
[b] Key Laboratory of Alpine Ecology, Institute of Tibetan Plateau Research, Chinese Academy of Sciences, Beijing, 100085, China
[c] State Key Laboratory of Environmental Geochemistry, Institute of Geochemistry, Chinese Academy of Sciences, Guiyang, 550081, China
[d] State Key Laboratory of Vegetation and Environment Change, Institute of Botany, Chinese Academy of Sciences, Beijing, 100093, China

ARTICLE INFO

Article history:
Received 1 March 2020
Received in revised form
19 June 2020
Accepted 19 June 2020
Available online 25 June 2020

Keywords:
Soil mercury
Grassland
Tibetan Plateau
Soil organic carbon
Atmospheric deposition

ABSTRACT

Soils, especially permafrost in the Arctic and the Tibetan Plateau, are one of the largest reservoirs of mercury (Hg) in the global environment. The Hg concentration in the grassland soils over the Tibetan Plateau and its driving factors have been less studied. This study analyzes soil total mercury (STHg) concentrations and its vertical distribution in grassland soil samples collected from the Tibetan Plateau. We adopt a nested-grid high-resolution GEOS-Chem model to simulate atmospheric Hg deposition. The relationship between STHg and soil organic carbon (SOC), as well as atmospheric deposition, are explored. Our results show that the STHg concentrations in the Tibetan Plateau are 19.8 ± 12.2 ng/g. The concentrations are higher in the south and lower in the north in the Tibetan Plateau, consistent with the previous results. Our model shows that the average deposition flux of Hg is 3.3 μg m^{-2} yr^{-1}, with 57% contributed by dry deposition of elemental mercury (Hg^0), followed by dry (19%) and wet (24%) deposition of divalent mercury. We calculate the Hg to carbon ratio ($R_{Hg:C}$) as 5.6 ± 6.5 μg Hg/g C, and the estimated STHg is 86.6 ± 101.2 Gg in alpine grasslands in the Tibetan Plateau. We find a positive relationship between STHg and SOC in the Tibetan Plateau (r^2 = 0.36) and a similar positive relationship between STHg and atmospheric total Hg deposition (r^2 = 0.24). A multiple linear regression involving both variables better model the observed STHg (r^2 = 0.42). We conclude that SOC and atmospheric deposition influence STHg simultaneously in this region. The data provides information to quantify the size of the soil Hg pool in the Tibetan Plateau further, which has important implications for the Hg cycles in the permafrost regions as well as on the global scale.

1. Introduction

Mercury (Hg) is a toxic heavy metal that is associated with cardiovascular effects in adults and neurocognitive defects in fetuses (Koos and Longo, 1976). Mercury in the environment is emitted by both natural sources such as biomass burning and volcanism and anthropogenic sources such as fossil fuel combustion, artisanal gold mining, metal smelting, and industrial production (Pacyna et al., 2010; UNEP, 2013). Once released into the atmosphere, it is transported and recycled among air, soil, and water and eventually removed from the surface environment through burial in deep ocean sediments and subsurface soils (Amos et al., 2014; Selin, 2009).

Soil plays an important role in the global biogeochemical cycling of Hg and serves both as a source and a sink of Hg in the atmosphere (Grigal, 2003). Mercury in the soil originates from the weathering of parent rock, vegetation-fall, and direct atmospheric deposition (Stein et al., 1996; Zhou et al., 2018). When the Hg from atmospheric deposition and vegetation-fall is input to the soil, it is combined with soil organic carbon (SOC) (Obrist et al., 2017). Loss of Hg from soil includes evasion to the atmosphere after the combined SOC is decomposed by microorganisms and leaching with dissolved organic carbon into runoff or soil solution (Åkerblom et al., 2008; Kocman et al., 2011). The forms, sorption, and transformation of soil Hg are influenced by the amount and composition of soil organic matter, oxidized minerals, as well as soil pH and redox conditions (O'Connor et al., 2019; Beckers and Rinklebe, 2017). In cold regions, Hg can be frozen into the permafrost

☆ This paper has been recommended for acceptance by Jörg Rinklebe.
* Corresponding author.
E-mail address: zhangyx@nju.edu.cn (Y. Zhang).

https://doi.org/10.1016/j.envpol.2020.115079
0269-7491/

because of stagnant microbial activity. Soils in permafrost regions are estimated to hold 1656 ± 962 Gg of Hg, of which 793 ± 461 Gg (48%) is stored in the permafrost (Schuster et al., 2018). Mercury isotope data suggest that 1088 ± 379 Gg of Hg are stored in the surface soil globally, of which 7% is stored in the tundra soils (Wang et al., 2019). Permafrost degradation associated with climate warming resumes soil microbial activity, which largely accelerates the release of Hg to the atmosphere and rivers (Li et al., 2012; Wang et al., 2006; Yang et al., 2007; Lim et al., 2019; Schuster et al., 2011; Fisher et al., 2012). This could serve as an important source of Hg into the atmosphere and has a substantial impact on the global Hg cycle (Obrist et al., 2017; Schuster et al., 2018; Mu et al., 2020).

The Hg concentrations in soil are largely influenced by the SOC content, and significantly positive correlations have been identified between soil total Hg concentrations (STHg) and SOC worldwide (Grigal, 2003; Obrist et al., 2011). This is because of the high affinity of divalent Hg to appropriate receptor sites in organic molecules, such as forest soils and agricultural soils (O'Connor et al., 2019; Beckers and Rinklebe, 2017). Thus, the SOC provides a good indicator of the number of receptor sites and how much Hg can be retained (i.e., receptor-limited regime) (Schuster et al., 2018). Except this, mercury to carbon ratio ($R_{Hg:C}$) also provides a useful normalized tracer of the driving factors of Hg contamination. Changes in $R_{Hg:C}$ in different soils reveal that STHg concentrations are influenced by parent rock and/or atmospheric input (Xue et al., 2019). So far, most studies only focus on the influence of SOC on STHg, but the role of atmospheric input is less quantitatively studied.

The Tibetan Plateau, known as the 'Third Pole', is one of the most remote and cold regions in the world that accounts for about three-quarters of alpine permafrost in the Northern Hemisphere (Wang and French, 1995). The Tibetan Plateau is a pristine area with negligible local sources, but sensitive to anthropogenic impacts (Yao et al., 2012), especially input of Hg transported from nearby populous and industrialized regions in India (Huang et al., 2016). The Tibetan Plateau also receives deposition from the Northern Hemispheric background air with Hg from long-range sources (Wang et al., 2017). Sedimentary and glacier ice core records show that concentrations of Hg in the Tibetan Plateau substantially increase since the 1860s (500%, from about 0.5 ng L^{-1} to 3 ng L^{-1}) (Kang et al., 2016; Wang et al., 2010). The large permafrost mass and proximity to source regions make the Tibetan Plateau a unique geographical location to study the storage of soil Hg and its driving factors such as SOC and atmospheric input (Loewen et al., 2007). Previous studies have reported the concentrations and distribution of Hg in the surface soil (e.g., 0–20 cm) of the Tibetan Plateau (Zhu et al., 2014; Sheng et al., 2012), but data in the permafrost grassland soils are limited, especially for deeper layers. Here we provide new data on Hg of grassland soils in the Tibetan Plateau. We also evaluate the driving factors of Hg content in the soil and permafrost, including the SOC content and the atmospheric deposition of Hg from the GEOS-Chem model. The analysis is also extended to the whole country based on a compilation of literature data.

2. Methods

2.1. Sites and samples

The Tibetan permafrost regions are mainly covered by three grassland types (Fig. 1c), including Alpine Steppe (AS, dominant by *Stipe purpurea* and *Carex moorcroftii*), Alpine Meadow (AM, *Carex moorcroftii* and *Kobresia pygmaea*), and Swamp Meadow (SM, *K. humilis and K. tibetica*) (Yang et al., 2015). The climate is cold and dry across the Tibetan Plateau with mean annual temperature −4.9 to 6.1 °C and mean annual precipitation 84.3–593.9 mm, 90% of which falls from May to September (Ding et al., 2016). Similar to other permafrost regions around the world, Tibetan permafrost has experienced significant thaw, such as increased active layer thickness (Wu and Zhang, 2010) and thermal erosion (Ding et al., 2016). We used the 114 samples collected by Ding et al. (2016) during the summers (July and August) of 2013 and 2014 in the Tibetan Plateau (Fig. 1a). The detail of the sampling procedure has been described in Ding et al. (2016). Briefly, the sampling sites covered broad climatic gradients and major grassland types. Of all sampling sites, 52 sites were from AS, 55 sites were from AM, and 7 sites were from SM and all in permafrost or seasonal frozen regions. The altitude of the samples ranges 3000–5000 m with roughly similar samples (n = 37, 16, 31, and 28) in four subgroups (<3500 m, 3500–4000 m, 4000–4500 m, and >4500 m, respectively) (Fig. 1b). At each site, five 1 m × 1 m quadrats were set up, locating at each corner and the center of a 10 m × 10 m plot. For each quadrat, aboveground biomass was clipped at the ground level and pooled. Pedon samples were collected within three quadrats along a diagonal line of the plot. Three samples for each site (a total of 342 boreholes from 114 sites) were drilled at 10 depths. In the laboratory, all samples were dried indoor for 48 h and stored in a refrigerator under dark conditions. The samples are sieved (2 mm mesh) and handpicked to remove fine roots for subsequent measurements. In this study, we used samples from five depths (0–10 cm, 10–20 cm, 50–70 cm, 150–200 cm, and 250–300 cm). One limitation of this study is the lack of active layer depth and age-depth data of individual sites. Given that the average active layer thickness is 2.4 m with a range of 1.3–3.5 m along the Tibetan Plateau (Pang et al., 2009), we consider the fifth layer as the 'permafrost layer' and above four as 'active layer' as an approximation.

2.2. Mercury analysis and quality assurance and quality control

The Hg concentrations of soil samples were analyzed by a Direct Mercury Analyzer (DMA-80 with T660, Milestone Srl, Italy) following the USA EPA method 7473. Controlled heating stages were implemented to first dry and then thermally decompose a sample introduced into a quartz tube. A continuous flow of air carried the decomposition products through a catalyst bed where interferences, like halogens or nitrogen/sulfur oxides, are trapped. All Hg species were reduced to elemental Hg and were then carried along to a gold amalgamator where the Hg was selectively collected. The system was purged and the amalgamator was subsequently heated to release all Hg vapors to the single beam, fixed wavelength atomic absorption spectrophotometer. The absorbance measured at 253.7 nm was proportional to Hg content in the sample.

Soil total Hg quantification was performed employing calibration curves with certified materials. Standard reference materials were GBW07423 from the National Research Center for Certified Reference Materials, China. The standard value of standard reference materials is 32 ± 3 ng/g, while the test value was 31.6 ± 1.7 ng/g and the recovery rate was 98.9%. Curves were considered optimal if the regression coefficient was ≥0.99. The instrument detection limit (IDL) was calculated based on three times the standard deviation of blanks, consisting of empty preheated combustion boats. The IDL for this method is 0.0005 ng Hg/1.0 g soil, below the lowest STHg measured for all samples (2.8 μg/kg). The median of relative standard deviation (RSD) in triplicate analyses of subsamples collected from individual sample sites is 11%.

2.3. Atmospheric model

We use the GEOS-Chem nested-grid Hg model (version 12.1.0, http://acmg.seas.harvard.edu/geos), which is run during

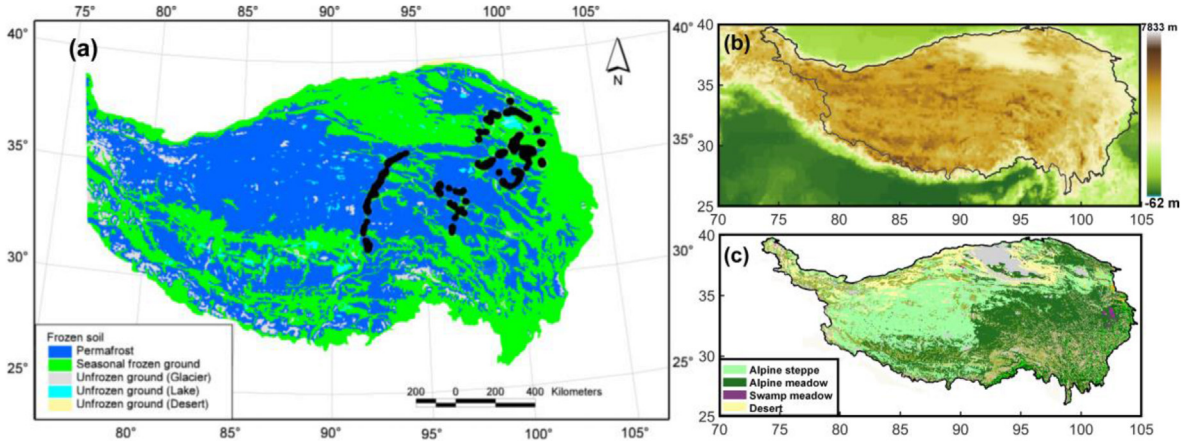

Fig. 1. (a) Sampling sites (black dots) (Ding et al., 2016) and soil types in the Tibetan Plateau (Li and Cheng, 1996); (b) Altitude map of Tibetan Plateau [The Global Land One-kilometer Base Elevation (GLOBE) Digital Elevation Model, Version 1.0. National Oceanic and Atmospheric Administration]; (c) Vegetation map of Tibetan Plateau (China's Vegetation Atlas with 1:1000000, Chinese Academy of Science, 2001).

2015–2016 with the previous 1 year as spin-up. The results from the global (4 × 5°) Hg simulation are used as initial and boundary conditions for a nested-grid simulation over the Asian domain (defined as 15–55°N and 70–140°E). The nested model is driven by GEOS-FP meteorological fields at a horizontal resolution 0.25° latitude × 0.3125° longitude. Both the nested and global models have 47 vertical layers. This one-way nesting approach has been applied to understand Hg chemistry and transport over North America and East Asia and the simulation results are in good agreement with the observation (Wang et al., 2014; Zhang, Y. et al., 2012). The model includes three tracers: gaseous elemental mercury, Hg^0, and gaseous and particulate-bound divalent mercury, Hg^{II}, and Hg^P, respectively. In the model, Hg^0 is emitted by natural and anthropogenic sources, while Hg^{II} and Hg^P are emitted only by anthropogenic sources (Zhang et al., 2016). Hg^{II} and Hg^P undergo wet and dry deposition, and Hg^0 subjects to dry deposition (Selin, 2009). Re-emissions of Hg^0 from terrestrial and oceanic reservoirs are also included (Holmes et al., 2010; Horowitz et al., 2017). The re-emission fluxes are modeled as functions of environmental parameters (e.g., temperature, wind speed, and short-wave radiation) and soil and oceanic Hg concentrations, which are not dynamically traced by the model but specified with observational data. Divalent mercury (i.e. Hg^{II} and Hg^P) follows an empirical gas-particle partitioning relationship based on air temperature and aerosol concentration, following Amos et al. (2012). The model also considers redox reactions between Hg^0 and Hg^{II} that include two-stage oxidization of Hg^0 initialized by Br atom, and photo-reduced reduction of Hg^{II} to Hg^0 in cloud droplets (Horowitz et al., 2017). We use the model output of atmospheric Hg deposition data, including the dry and wet deposition of Hg^0, Hg^{II}, and Hg^P. The spatial distribution of atmospheric deposition is compared against soil Hg concentrations to evaluate its role in influencing the latter.

2.4. Statistics and dataset

Grubbs' test was used to find if a minimum value or a maximum value of STHg or $R_{Hg:C}$ is an outlier (GB/T4883-2008). A two-way analysis of Variance (ANOVA) followed by Tukey multiple comparisons (software: Matlab R2018a) was applied for comparisons among multiple groups of samples. The criterion of significance was set at $p < 0.05$. The linear regression analysis was used to study the relationship between STHg versus deposition and SOC (software: Matlab R2018a). We included the SOC data analyzed by Ding et al. (2016) for the samples we measured STHg. We also collected literature data on SOC and STHg in different soil types in China (Fig. S4, Fig. S5, Table S2, refer to SI for a complete reference list). It resulted in 920 data points covering the Tibetan Plateau, North, Northeast, Central, East, Southeast, and Southwest China. These samples are from agricultural fields (491 points), urban regions (95 points), and mining areas (97 points). A Monte Carlo approach was used for uncertainty analysis of Hg storage estimate (Rubinstein and Kroese, 2008). The Hg storage was calculated as the product of carbon storage and Hg to carbon ratio ($R_{Hg:C}$). The calculation was repeated for a million times with randomly sampled carbon storage and $R_{Hg:C}$ data. The probability distribution of carbon storage of the Tibetan grassland soils is from Ding et al. (2016), while that of the latter is from this study. The Monte Carlo simulation was also conducted with Matlab R2018a.

3. Results and discussion

3.1. Concentrations and distribution of soil mercury in the Tibetan Plateau

Fig. 2 shows the probability distribution of measured STHg concentrations at five depths. Generally, the STHg concentrations in the Tibetan Plateau are 19.8 ± 12.2 ng/g. The probability distributions of STHg are right-skewed with higher means than medians. About 60% of the STHg data are between 10 and 30 ng/g. Occasionally, there are samples with concentrations greater than 60 ng/g in deep layers (>150 cm). We find that the STHg concentrations in the Tibetan Plateau are about 50% lower than the tundra data over Alaska (43 ± 30 ng/g) and are similar to other regions in the Northern Hemisphere (20 ± 10 ng/g) (Schuster et al., 2018). Our surface layer (0–10 cm) data is slightly less than the data by Sheng et al. (37 ± 18 ng/g, 2012) in the southern part of the Tibetan Plateau but is slightly higher than Sun et al. (14.8 ± 5.5 ng/g, 2017) in the northeastern part of the Tibetan Plateau. Our results are also in agreement with the results (~25 ng/g STHg in grassland in the Tibetan Plateau) of Zhu et al. (2014). The STHg in the permafrost layer (18.7 ± 14.8 ng/g) is not significantly different from the active layer (20.0 ± 11.5 ng/g) (T-test, $p = 0.40$).

The STHg concentrations exhibit large spatial variability in the surface layer (0–10 cm) of the Tibetan plateau (Fig. 3a). Superimposed are the STHg data over the southern part of the Tibetan Plateau summarized by Sheng et al. (2012). Overall, the STHg concentrations on the Tibetan Plateau are higher in the south than in the north ($p < 0.01$), which is consistent with the results of Zhu

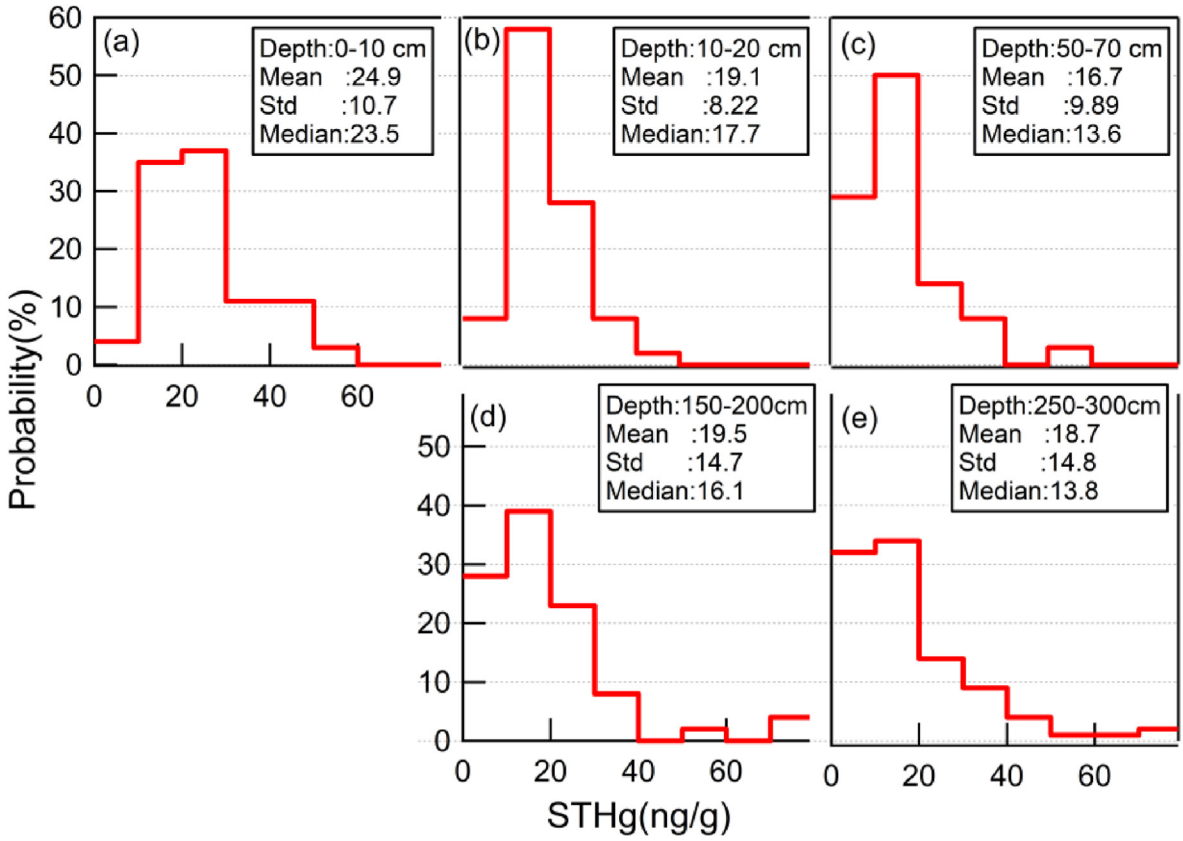

Fig. 2. Probability distribution of STHg in Tibetan grassland soils at different depth ranges: (a) 0–10 cm, (b) 10–20 cm, (c) 50–70 cm, (d) 150–200 cm and (e) 250–300 cm.

et al. (2014). This pattern is associated with the elevated anthropogenic Hg emissions in South Asia, which could be carried and subsequently deposited by the South Asian monsoon (Huang et al., 2019). The distribution of STHg concentrations in the deeper layers are similar to the surface layer: higher concentrations in the south than the north (Fig. 2b–e). This may be caused by the influence of atmospheric Hg input that penetrates to depth due to diffusion and leaching.

Fig. 4 shows the vertical profiles of STHg averaged for different grassland types and altitudes. Generally, the STHg concentrations decrease with depth in the top three layers (0–70 cm) and remain almost unchanged in below. We find relatively high STHg concentration in soil samples >20 cm depth of all grassland types. This pattern is consistent with the results of Sun et al. (2017), though their sample depth ranges from 0 to 60 cm and a slight increase of STHg was found in 40–60 cm depths. A similar decreasing trend with depth was also reported by Schuster et al. (2018). The STHg concentrations in SM are the largest among the three grasslands ($p < 0.05$, Fig. 4a, Table S1). For the three types of grassland sampled in this study, the medians of STHg concentrations (top 20 m) are 21.9 ng/g, 18.3 ng/g, and 30.8 ng/g in AM, AS, and SM, respectively. Our results in AM are similar to the data reported in Mu et al. (2020) (0–50 cm, 18.1 ng/g), and are higher for AS (6.48 ng/g), but lower for SM (37.6 ng/g). Although the absolute concentrations are different in the two studies, the trends among the types of grasslands are consistent. This trend also agrees with that of the average SOC in the three grassland types (Table 1): SM (2.1%) > AM (1.1%) > AS (0.6%).

We will elaborate on the influence of SOC on STHg in later sections. Previous studies found increasing trends of STHg with altitude due to the increase of atmospheric deposition (Zhang et al., 2013; Blackwell and Driscoll, 2015). We do not find a significant trend for STHg at different altitudes for different depth ranges (Fig. 4b and Table S1), even though the average temperature at different altitudes varies for ~10 °C given a temperature lapse rate of 0.6 °C per 100 m. It seems that temperature is not an important driving factor for STHg in the frozen soil in this region, as the microbial activity is paused under low temperature and STHg is fixed in the deep soil (Schirrmeister et al., 2011). The temperature also influences the productivity of overlying vegetation and further influences the SOC and STHg (Obrist et al., 2017), but this factor seems not significant for the three types of grasslands in this region.

3.2. Storage of soil mercury in the Tibetan Plateau

Table 1 shows the SOC, calculated $R_{Hg:C}$, and total Hg storage of four depths (0–50 cm, 50–100 cm, 100–200 cm, 200–300 cm) over different types of grasslands in the Tibetan Plateau. The average SOC over the whole soil profile is 0.9% (0–300 cm), with higher values in the upper profiles: 2.2%, 1.5%, and 1.1% in the top 50, 100, and 200 cm, respectively. The Tibetan SOC data is much lower than Schuster's (2018) over Alaska (all sample cores > 1% and 1/2 cores > 5%) and Olson's (2018) over Arctic tundra (~19%).

Ding et al. (2016) estimated the total organic carbon (OC) stock in alpine grasslands in the Tibetan Plateau (area: 1.1 million km^2) is 6.23 (5.33–7.30 as interquartile range, the same hereafter) Pg for the top 50 cm. This number increases to 8.51 (7.30–9.93) Pg, 12.2 (10.4–14.3) Pg and 15.3 (13.0–17.8) Pg if extending to a depth of 100 cm, 200 cm, and 300 cm, respectively. Generally, our estimate of $R_{Hg:C}$ value is 5.6 ± 6.5 μg Hg/g C (0–300 cm, with 5.1 ± 6.7 μg Hg/g C for the active layer and 7.5 ± 5.8 μg Hg/g C for the permafrost layer), higher than that of Schuster's data (1.8 ± 1.2 μg Hg/g C) in

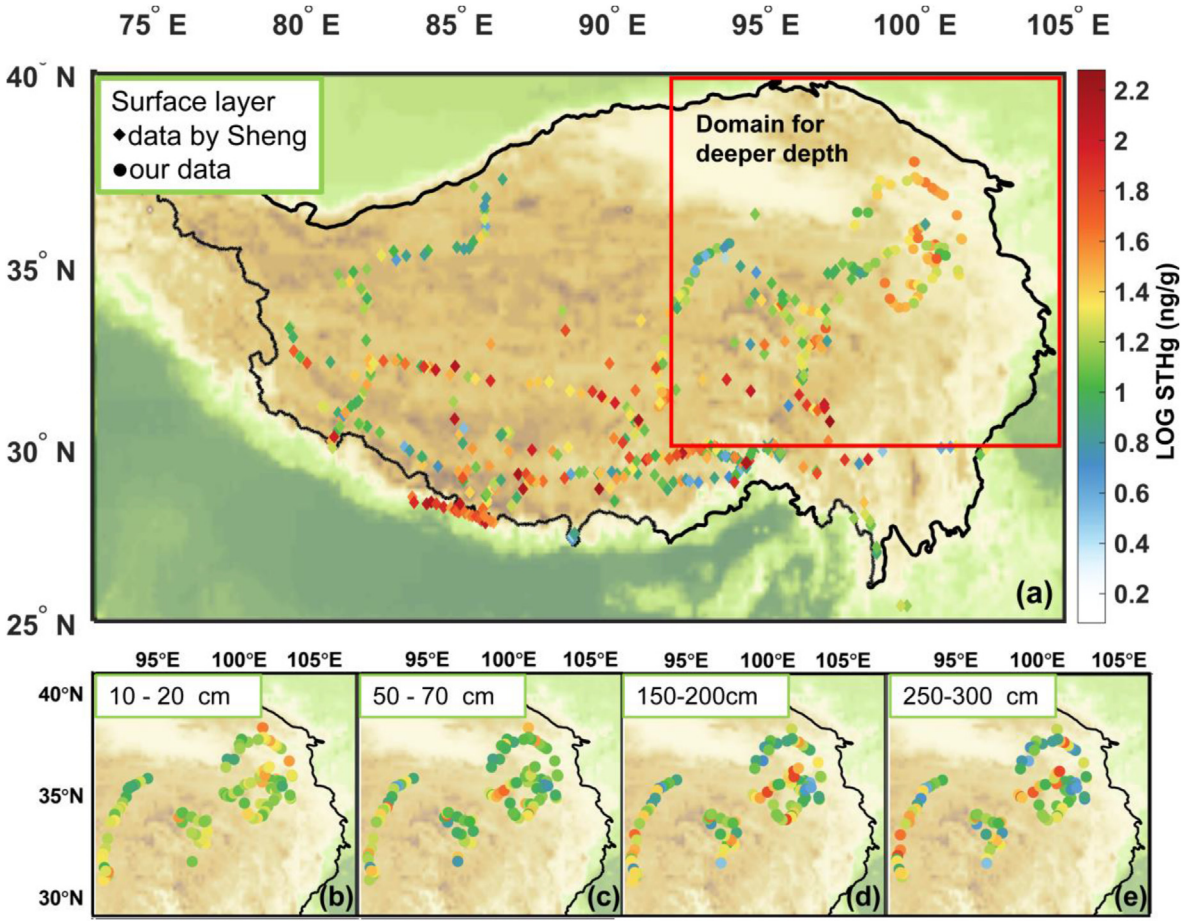

Fig. 3. Measured STHg for different depths in the Tibetan Plateau. (a) 0–10 cm [◆: data collected by Sheng et al. (2012)], (b) 10–20 cm, (c) 50–70 cm, (d) 150–200 cm and (e) 250–300 cm. The black line in panel a represents the boundary of the Tibetan Plateau. The background color represents the altitudes with increasing values from green to yellow. Note the domains of panels b–e are smaller than that of the panel a (shown as a red rectangle in panel a).

Alaska because of the relatively low SOC in the Tibetan Plateau (Schuster et al., 2018). This suggests substantial variability in $R_{Hg:C}$ values in different regions and terrestrial ecosystems. Indeed, the median of $R_{Hg:C}$ values over tundra from Olson et al. (0.27 μg Hg/g C, 2018) is also lower than that of Schuster et al. (2018). The average $R_{Hg:C}$ in western Siberia regions decreases from 0.38 μg Hg/g C in the active layer to 0.23 μg Hg/g C in permafrost region (Lim et al., 2020), which is lower than that of Schuster's (2018) and similar to Olson's (2018). Similarly, the $R_{Hg:C}$ values become smaller for the top 50 cm of our dataset as the SOC is higher.

By multiplying the OC stock and $R_{Hg:C}$ values, we estimate that the total Hg storage is 86.6 ± 101.2 Gg for the top 300 cm with 36.8 ± 44.9, 33.3 ± 36.5, and 7.9 ± 9.5 Gg from AM, AS, and SM grasslands, respectively. We calculate the Hg stocks per unit area are 0.08 Gg Hg/10^3 km^2 for AM, 0.05 Gg Hg/10^3 km^2 for AS, and 0.16 Gg Hg/10^3 km^2 for SM, consistent with the trend of SOC content, which indicates the influence of SOC on soil mercury. The Hg stock in the top 50 cm accounts for 11% of the total profile, which is lower than the fraction of soil layer depth (17%) reflecting the lower $R_{Hg:C}$ values in the top of soil profiles (Table 1). The STHg stock in the permafrost layer is 23.4 Gg, accounting for 27% of the total profile, with the remaining 73% (63.2 Gg) in the active layer. This ratio in permafrost is lower than Schuster's (2018) estimation in Northern Hemisphere permafrost regions (48%), but higher than the fraction (6%) in pan-Arctic soils given by Lim et al. (2020). Applying the $R_{Hg:C}$ values of Schuster et al. (2018), Lim et al. (2020), and Olson et al. (2018) to the carbon stock in Tibetan grassland results in a Hg mass of 27.7 ± 17.7 Gg, 7.4 ± 2.7 Gg, 6.6 ± 3.7 Gg, respectively, in the top 300 cm, which are much smaller than that using native values. Therefore, regional variabilities in $R_{Hg:C}$ values should be considered in evaluating the size of the global soil Hg reservoir.

3.3. Atmospheric Hg deposition in Tibetan Plateau

Fig. 5 shows the modeled atmospheric deposition of Hg in the Tibetan Plateau. The total atmospheric deposition in the Tibetan Plateau ranges 0.7–18 μg m^{-2} yr^{-1}. The average deposition flux of Hg is 3.3 μg m^{-2} yr^{-1}, with 57% contributed by dry deposition of Hg^0, followed by dry deposition of Hg^{II} and Hg^P (19%) and wet deposition (24%). Dry deposition and wet deposition show different spatial distribution patterns, especially in the southwestern Tibetan Plateau. The wet deposition is higher in the southern and northeastern parts of the Plateau but is very low over the western region. The precipitation in the Tibetan Plateau has an increasing trend from west to east and north to south. The maximum precipitation occurs in the southeastern region (Arcenegui et al., 2007), which is consistent with the spatial distribution of wet deposition of Hg. The dry deposition is high in the eastern part of the Plateau, which is associated with the relatively higher atmospheric Hg concentrations due to elevated anthropogenic emissions in Qinghai and Sichuan provinces. Compared with the extremely low wet

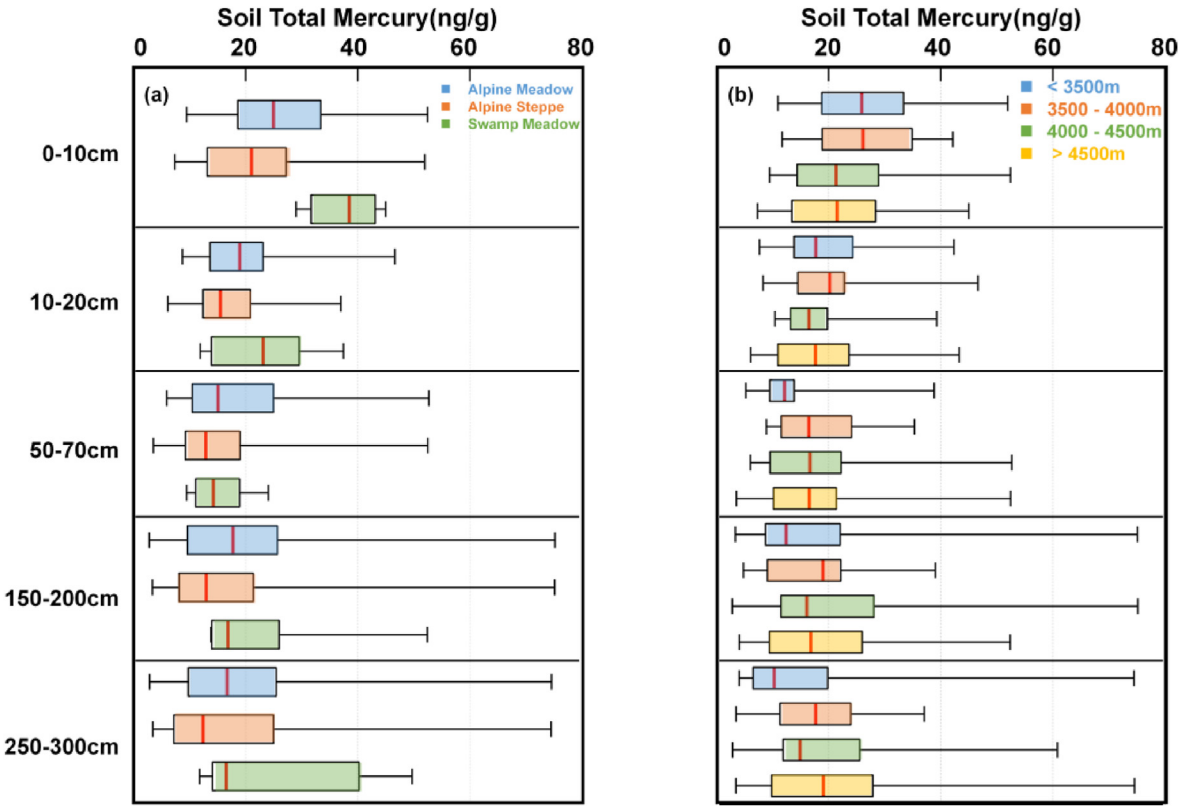

Fig. 4. (a)Vertical distributions of STHg of different grassland types. (AM: Alpine Meadow; AS: Alpine Steppe; SM: Swamp Meadow); (b) Vertical distributions of STHg of altitudes (altitude < 3500 m, 3500–4000 m, 4000–4500 m, > 4500 m).

Table 1
The SOC, $R_{Hg:C}$, and total Hg storage (mean ± standard deviation) in the Tibetan grassland soils.

Grasslands (Area: 10^3 km^2)	Depth range (cm)	SOC (%)	$R_{Hg:C}$ (μg Hg/g C)	Mercury stock (Gg Hg)
Alpine Meadow (453.1)	0–50	2.7 ± 1.3	1.1 ± 0.8	3.5 ± 2.4
	0–100	1.8 ± 1.4	2.4 ± 2.8	10.0 ± 11.7
	0–200	1.3 ± 1.4	4.9 ± 7.0	27.0 ± 38.5
	0–300	1.1 ± 1.3	5.6 ± 6.8	36.8 ± 44.9
Alpine steppe (640.0)	0–50	1.5 ± 1.0	1.9 ± 1.3	3.9 ± 2.7
	0–100	1.0 ± 0.9	3.6 ± 3.6	10.5 ± 10.6
	0–200	0.7 ± 0.8	5.6 ± 6.6	23.9 ± 28.2
	0–300	0.6 ± 0.8	6.0 ± 6.5	33.3 ± 36.5
Swamp Meadow (50.9)	0–50	5.1 ± 2.7	0.6 ± 0.3	0.7 ± 0.4
	0–100	3.2 ± 2.5	0.8 ± 0.3	1.2 ± 0.5
	0–200	2.5 ± 2.5	2.1 ± 3.5	5.5 ± 9.5
	0–300	2.1 ± 2.4	2.4 ± 3.2	7.9 ± 9.5
Total (1144.0)	0–50	2.2 ± 1.5	1.5 ± 1.1	9.2 ± 7.0
	0–100	1.5 ± 1.4	2.8 ± 3.2	24.8 ± 27.8
	0–200	1.1 ± 1.3	5.1 ± 6.7	63.2 ± 82.2
	0–300	0.9 ± 1.2	5.6 ± 6.5	86.6 ± 101.2

deposition, the dry deposition is relatively high over the southwestern Plateau, where the Hg^{II} concentrations are higher due to high altitudes. The observations for Hg deposition flux are rather limited over the Tibetan Plateau. The wet deposition fluxes of total Hg at Nam Co alpine site were reported as 1.75 μg m^{-2} yr^{-1} from 2009 to 2011 (Huang et al., 2012), which is higher than the model results in 2015–2016 (0.76 μg m^{-2} yr^{-1}). The average Hg accumulation rates obtained from the 15 glacier ice cores is about 3.1 μg m^{-2} yr^{-1} (Kang et al., 2016; Zhang, Q. et al., 2012), which is similar to our model results (3.3 μg m^{-2} yr^{-1}). The sediment core records (18.2 μg m^{-2} yr^{-1}) are also consistent with the GEOS-Chem model results (16.3 μg m^{-2} yr^{-1}) (Kang et al., 2016). Due to the lack of measurement data, we focus on the relative spatial pattern of modeled Hg deposition, instead of the absolute amount.

3.4. Driving factors of STHg in Tibetan Plateau

Similar to previous studies (e.g. Obrist et al., 2011; Sun et al., 2017), a linear relationship between STHg and SOC for the Tibetan grassland soil samples in the top 10 cm (log-transformed, F-test: $p < 0.01$) (Fig. 6a):

$$\log(\mathrm{STHg}) = 0.30 \log(\mathrm{SOC}) + 1.3,\ r^2 = 0.36 \quad (1)$$

As the depth increases, this linear relationship becomes weaker

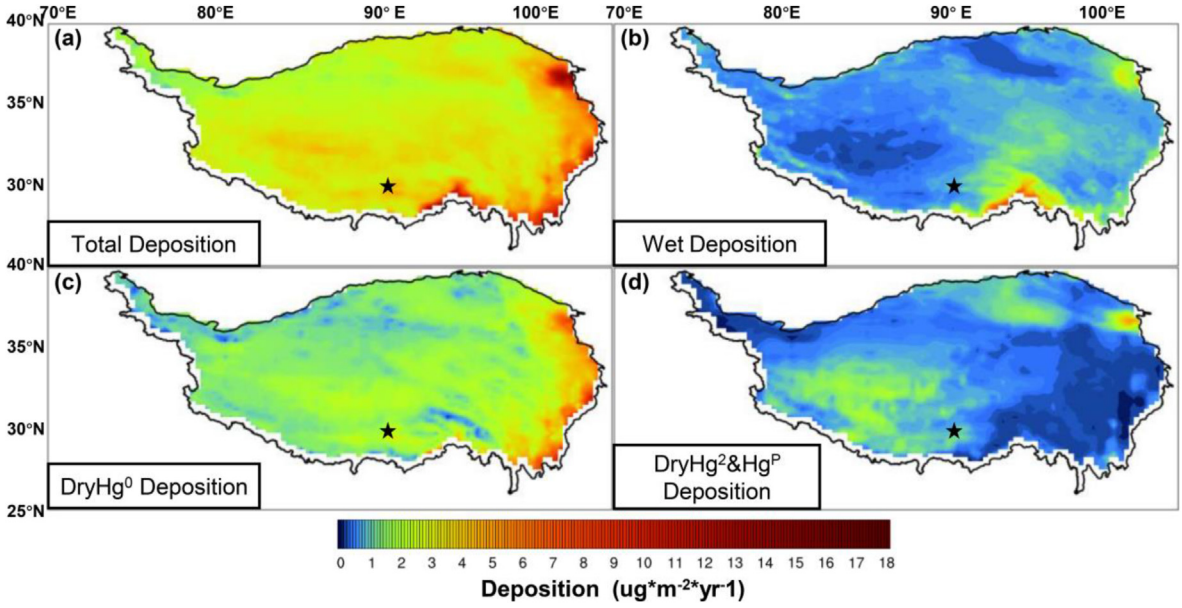

Fig. 5. Estimated mercury depositions for types at the Tibetan Plateau. (a) total deposition, (b) wet deposition, (c) dry deposition of Hg^0, (d) dry deposition of Hg^2 and Hg^P (black pentagram represents Lhasa).

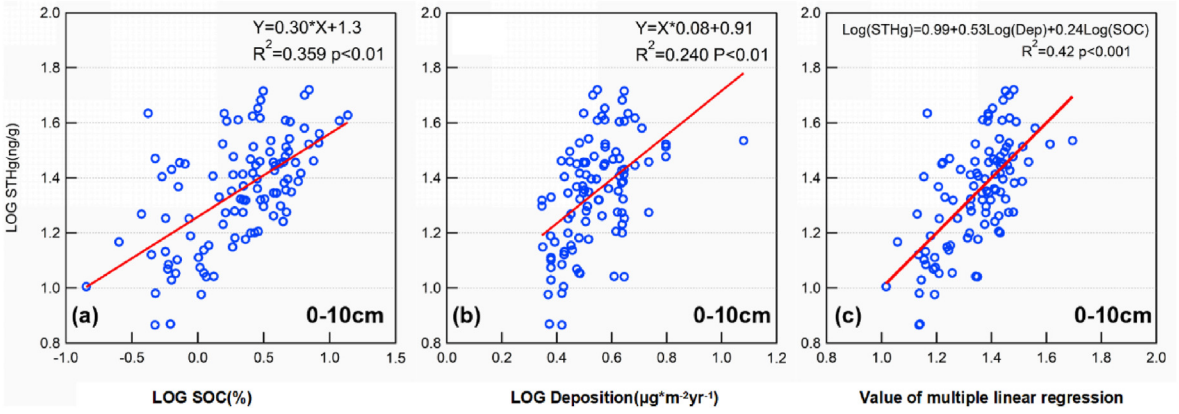

Fig. 6. (a) Linear regression of STHg and SOC on Tibetan Plateau (in log scale, 0–10 cm); (b) Linear regression of STHg and atmospheric deposition on Tibetan Plateau (in log scale, 0–10 cm); (c) Multiple-variable linear regression of STHg and both SOC and atmospheric deposition (in log scale, 0–10 cm).

(Fig. S1). The coefficients of determination (r^2) decrease to 0.13 in the 10–20 cm depth, and less than 0.1 in the deeper samples. The relationships also become not significant for samples below 50 cm depth.

We find a linear relationship between STHg and atmospheric deposition (log-transformed, F-test: $p < 0.01$) (Fig. 6b):

$$\log(\mathrm{STHg}) = 0.09\log(\mathrm{Dep}) + 0.91,\ r^2 = 0.24 \quad (2)$$

Similarly, we find the surface soil is more affected by atmospheric deposition than the deeper layers. The linear relationship between deposition and STHg is weaker in deeper soils. Similar to the relationship with SOC, the coefficients of determination (r^2) decrease to 0.12 in the 10–20 cm depth, and less than 0.1 in the deeper samples. The relationships also become not significant for samples below 50 cm depth (Fig. S2).

Even though the atmospheric deposition appears to have little to no influence on STHg below 50 cm depth, we find a good linear relationship between the STHg concentrations in a layer and the layer above (Fig. S3, $r^2 = 0.52$, 0.18, 0.49, and 0.76, for the second to the fifth layer, respectively). Combined with the relationship between deposition and STHg in each layer, we conclude that the STHg in deeper layers is more influenced by factors such as parent rock Hg content, and leaching from above layers (Wang et al., 2019).

Schuster et al. (2018) proposed receptor-limited and flux-limited regimes for the relationship between SOC and STHg. They assumed a threshold value of 10% for SOC: if SOC <10%, the number of receptor sites limit the Hg can retain (i.e., receptor-limited regime); if SOC > 10%, receptor sites appear unlimited and the flux of Hg from the atmosphere limits the STHg (i.e., flux-limited regime). However, from our analysis, we do not see such a threshold for Tibetan Plateau grassland soils, but the atmospheric deposition even influences soils with SOC <10%. We find a multi-linear regression with both SOC and deposition could better explain the variability of observed STHg ($r^2 = 0.42$, Fig. 6c):

$$\log(\mathrm{STHg}) = 0.53\log(\mathrm{Dep}) + 0.24\log(\mathrm{SOC}) + 0.99,\ r^2 = 0.42 \quad (3)$$

We thus conclude that SOC and atmospheric deposition work

simultaneously in this region. We also tried to incorporate depth as the third variable for our regression model, but it does not increase the r^2 value. Furthermore, the weaker relationship between STHg and SOC and deposition fluxes suggest other influencing factors in the deep layer soils, such as the contribution from parent rock and leaching from upper soil profiles.

4. Summary

This study finds that the mean total STHg concentrations in the Tibetan Plateau grassland surface soils are 19.8 ± 12.2 ng/g. The concentrations exhibit large spatial variability, higher in the south/east and lower in the north/west. The concentrations decrease with depth in the top 70 cm but remain almost unchanged in below. We find that the swamp meadow STHg concentrations are the largest among the three types of grasslands, consistent with the trends in SOC. The mean $R_{Hg:C}$ of our samples is 5.6 ± 6.5 μg Hg/g C and the estimated Hg mass is 86.6 ± 101.2 Gg in grassland soils of the Tibetan Plateau. Among other influencing factors such as Hg content in parent rocks, we find SOC and atmospheric deposition both influence STHg.

We find different $R_{Hg:C}$ values compared to other regions, indicating the importance of regional variability of $R_{Hg:C}$ values in estimating global Hg mass based on carbon mass. This highlights the importance of our dataset in further qualifying soil Hg stocks in the Tibetan Plateau as well as on a global scale. Despite the large global mass of Hg in soils, the transport and fate of Hg in this reservoir is not fully understood. Especially, how SOC content influences the STHg and its interaction with atmospheric Hg deposition remain unclear. Process-based models considering the soil-air exchange of Hg and its transformation and vertical transport in soil columns are needed to test different hypotheses such as those brought up by Schuster et al. (2018) and this study. Our findings provide valuable data to evaluate and calibrate models developed for this research.

We note a large range of uncertainty associated with our estimate of Hg storage in Tibetan grassland soils (86.6 ± 101.2 Gg for the top 300 cm). This uncertainty derives from both the estimate of carbon storage and the $R_{Hg:C}$ values. To increase sample size and cover more representative land types help to reduce such uncertainty. However, the general poor linear relationships between STHg and SOC and atmospheric deposition are the major limitation for this approach, despite its wide application in the literature. More factors, such as SOC characteristics, soil microbial activities, STHg chemical composition, metrological factors, active layer depth, and parent rock characteristics, should be included and analyzed for their roles in driving the variability of STHg in future studies.

CRediT authorship contribution statement

Jing Gu: Methodology, Software, Validation, Investigation, Writing - original draft. **Qiaotong Pang:** Validation, Investigation. **Jinzhi Ding:** Validation, Investigation. **Runsheng Yin:** Resources, Data curation. **Yuanhe Yang:** Resources. **Yanxu Zhang:** Conceptualization, Methodology, Writing - review & editing, Supervision, Project administration, Funding acquisition.

Declaration of competing interest

We declare that we do not have any commercial or associative interest that represents a conflict of interest in connection with the work submitted.

Acknowledgment

The authors gratefully acknowledge financial support from National Natural Science Foundation of China (NNSFC) 41875148, Start-up fund of the Thousand Youth Talents Plan, Jiangsu Innovative and Entrepreneurial Talents Plan, and the Collaborative Innovation Center of Climate Change, Jiangsu Province.

Appendix A. Supplementary data

Supplementary data to this article can be found online at https://doi.org/10.1016/j.envpol.2020.115079.

References

Åkerblom, S., Meili, M., Bringmark, L., Johansson, K., Kleja, D.B., Bergkvist, B., 2008. Partitioning of Hg between solid and dissolved organic matter in the humus layer of boreal forests. Water Air Soil Pollut. 189, 239–252. https://doi.org/10.1007/s11270-007-9571-1.

Amos, H.M., Jacob, D.J., Holmes, C.D., Fisher, J.A., Wang, Q., Yantosca, R.M., Corbitt, E.S., Galarneau, E., Rutter, A.P., Gustin, M.S., Steffen, A., Schauer, J.J., Graydon, J.A., St Louis, V.L., Talbot, R.W., Edgerton, E.S., Zhang, Y., Sunderland, E.M., 2012. Gas-particle partitioning of atmospheric Hg(II) and its effect on global mercury deposition. Atmos. Chem. Phys. 12, 591–603. https://doi.org/10.5194/acp-12-591-2012.

Amos, H.M., Jacob, D.J., Kocman, D., Horowitz, H.M., Zhang, Y., Dutkiewicz, S., Horvat, M., Corbitt, E.S., Krabbenhoft, D.P., Sunderland, E.M., 2014. Global biogeochemical implications of mercury discharges from rivers and sediment burial. Environ. Sci. Technol. 48, 9514–9522. https://doi.org/10.1021/es502134t.

Arcenegui, V., Guerrero, C., Mayoral, A.M., Morales, J., González, J., García-Orenes, F., Gómez, I., 2007. Water repellency under different plant species in a calcareous forest soil in a semiarid Mediterranean environment. Hydrol. Process. 2309, 2300–2309. https://doi.org/10.1002/hyp.

Beckers, F., Rinklebe, J., 2017. Cycling of mercury in the environment: sources, fate, and human health implications: a review. Crit. Rev. Environ. Sci. Technol. 47, 693–794. https://doi.org/10.1080/10643389.2017.1326277.

Blackwell, B.D., Driscoll, C.T., 2015. Deposition of mercury in forests along a montane elevation gradient. Environ. Sci. Technol. 49, 5363–5370. https://doi.org/10.1021/es505928w.

Chinese Academy of Sciences, 2001. Vegetation Atlas of China. Science Press, Beijing (in Chinese).

Ding, J., Li, F., Yang, G., Chen, L., Zhang, B., Liu, L., Fang, K., Qin, S., Chen, Y., Peng, Y., Ji, C., He, H., Smith, P., Yang, Y., 2016. The permafrost carbon inventory on the Tibetan Plateau: a new evaluation using deep sediment cores. Global Change Biol. 22, 2688–2701. https://doi.org/10.1111/gcb.13257.

Fisher, J.A., Jacob, D.J., Soerensen, A.L., Amos, H.M., Steffen, A., Sunderland, E.M., 2012. Riverine source of Arctic Ocean mercury inferred from atmospheric observations. Nat. Geosci. 5, 499–504. https://doi.org/10.1038/ngeo1478.

Grigal, D.F., 2003. Mercury sequestration in forests and peatlands: a review. J. Environ. Qual. 32, 393–405.

Holmes, C.D., Jacob, D.J., Corbitt, E.S., Mao, J., Yang, X., Talbot, R., Slemr, F., 2010. Global atmospheric model for mercury including oxidation by bromine atoms. Atmos. Chem. Phys. 10, 12037–12057. https://doi.org/10.5194/acp-10-12037-2010.

Horowitz, H.M., Jacob, D.J., Zhang, Y., DIbble, T.S., Slemr, F., Amos, H.M., Schmidt, J.A., Corbitt, E.S., Marais, E.A., Sunderland, E.M., 2017. A new mechanism for atmospheric mercury redox chemistry: implications for the global mercury budget. Atmos. Chem. Phys. 17, 6353–6371. https://doi.org/10.5194/acp-17-6353-2017.

Huang, J., Kang, S., Tian, L., Guo, J., Zhang, Q., Cong, Z., Sillanpää, M., Sun, S., Tripathee, L., 2016. Influence of long-range transboundary transport on atmospheric water vapor mercury collected at the largest city of Tibet. Sci. Total Environ. 566 (567), 1215–1222. https://doi.org/10.1016/j.scitotenv.2016.05.177.

Huang, J., Kang, S., Yin, R., Guo, J., Lepak, R., Mika, S., Tripathee, L., Sun, S., 2019. Mercury isotopes in frozen soils reveal transboundary atmospheric mercury deposition over the Himalayas and Tibetan Plateau. Environ. Pollut. https://doi.org/10.1016/j.envpol.2019.113432.

Huang, J., Kang, S., Zhang, Q., Yan, H., Guo, J., Jenkins, M.G., Zhang, G., Wang, K., 2012. Wet deposition of mercury at a remote site in the Tibetan Plateau: concentrations, speciation, and fluxes. Atmos. Environ. 62, 540–550. https://doi.org/10.1016/j.atmosenv.2012.09.003.

Kang, S., Huang, J., Wang, F., Zhang, Q., Zhang, Y., Li, C., Wang, L., Chen, P., Sharma, C.M., Li, Q., Sillanpää, M., Hou, J., Xu, B., Guo, J., 2016. Atmospheric mercury depositional chronology reconstructed from lake sediments and ice core in the Himalayas and Tibetan plateau. Environ. Sci. Technol. 50, 2859–2869. https://doi.org/10.1021/acs.est.5b04172.

Kocman, D., Kanduč, T., Ogrinc, N., Horvat, M., 2011. Distribution and partitioning of mercury in a river catchment impacted by former mercury mining activity. Biogeochemistry 104, 183–201. https://doi.org/10.1007/s10533-010-9495-5.

Koos, B.J., Longo, L.D., 1976. Mercury toxicity in the pregnant woman, fetus, and newborn infant: a review. Am. J. Obstet. Gynecol. 126, 390–409. https://doi.org/

10.1016/0002-9378(76)90557-3.
Li, R., Zhao, L., Ding, Y.J., Wu, T.H., Xiao, Y., Du, E.J., Liu, G.Y., Qiao, Y.P., 2012. Temporal and spatial variations of the active layer along the Qinghai-Tibet Highway in a permafrost region. Chin. Sci. Bull. 57, 4609–4616. https://doi.org/10.1007/s11434-012-5323-8.
Li, S., Cheng, G., 1996. Map of Frozen Ground on Qinghai -Xizang Plateau. Gansu Culture Press, Lanzhou (in Chinese).
Lim, A., Jiskra, M., Sonke, J., Loiko, S., Kosykh, N., Pokrovsky, O., 2020. A revised northern soil Hg pool, based on western Siberia permafrost peat Hg and carbon observations. Biogeosci. Discuss. 1–35. https://doi.org/10.5194/bg-2019-483.
Lim, A.G., Sonke, J.E., Krickov, I.V., Manasypov, R.M., Loiko, S.V., Pokrovsky, O.S., 2019. Enhanced particulate Hg export at the permafrost boundary, western Siberia. Environ. Pollut. 254, 113083 https://doi.org/10.1016/j.envpol.2019.113083.
Loewen, M., Kang, S., Armstrong, D., Zhang, Q., Tomy, G., Wang, F., 2007. Atmospheric transport of mercury to the Tibetan Plateau. Environ. Sci. Technol. 41, 7632–7638. https://doi.org/10.1021/es0710398.
Mu, C., Schuster, P.F., Abbott, B.W., Kang, S., Guo, J., Sun, S., Wu, Q., Zhang, T., 2020. Permafrost degradation enhances the risk of mercury release on Qinghai-Tibetan Plateau. Sci. Total Environ. 708, 135127 https://doi.org/10.1016/j.scitotenv.2019.135127.
O'Connor, D., Hou, D., Ok, Y.S., Mulder, J., Duan, L., Wu, Q., Wang, S., Tack, F.M.G., Rinklebe, J., 2019. Mercury speciation, transformation, and transportation in soils, atmospheric flux, and implications for risk management: a critical review. Environ. Int. 126, 747–761. https://doi.org/10.1016/j.envint.2019.03.019.
Obrist, D., Agnan, Y., Jiskra, M., Olson, C.L., Colegrove, D.P., Hueber, J., Moore, C.W., Sonke, J.E., Helmig, D., 2017. Tundra uptake of atmospheric elemental mercury drives Arctic mercury pollution. Nature 547, 201–204. https://doi.org/10.1038/nature22997.
Obrist, D., Johnson, D.W., Lindberg, S.E., Luo, Y., Hararuk, O., Bracho, R., Battles, J.J., Dail, D.B., Edmonds, R.L., Monson, R.K., Ollinger, S.V., Pallardy, S.G., Pregitzer, K.S., Todd, D.E., 2011. Mercury distribution across 14 U.S. Forests. Part I: spatial patterns of concentrations in biomass, litter, and soils. Environ. Sci. Technol. 45, 3974–3981. https://doi.org/10.1021/es104384m.
Olson, C., Jiskra, M., Biester, H., Chow, J., Obrist, D., 2018. Mercury in active-layer tundra soils of Alaska: concentrations, pools, origins, and spatial distribution. Global Biogeochem. Cycles 32, 1058–1073. https://doi.org/10.1029/2017GB005840.
Pacyna, E.G., Pacyna, J.M., Sundseth, K., Munthe, J., Kindbom, K., Wilson, S., Steenhuisen, F., Maxson, P., 2010. Global emission of mercury to the atmosphere from anthropogenic sources in 2005 and projections to 2020. Atmos. Environ. 44, 2487–2499. https://doi.org/10.1016/j.atmosenv.2009.06.009.
Pang, Q., Cheng, G., Li, S., Zhang, W., 2009. Cold regions science and technology active layer thickness calculation over the Qinghai – Tibet plateau. Cold Reg. Sci. Technol. 57, 23–28. https://doi.org/10.1016/j.coldregions.2009.01.005.
Rubinstein, R.Y., Kroese, D.P., 2008. Simulation and the Monte Carlo Method, second ed. John Wiley & Sons, Inc, New York.
Schirrmeister, L., Grosse, G., Wetterich, S., Overduin, P.P., Strauss, J., Schuur, E.A.G., Hubberten, H.W., 2011. Fossil organic matter characteristics in permafrost deposits of the northeast Siberian Arctic. J. Geophys. Res. Biogeosci. 116 https://doi.org/10.1029/2011JG001647.
Schuster, P.F., Schaefer, K.M., Aiken, G.R., Antweiler, R.C., Dewild, J.F., Gryziec, J.D., Gusmeroli, A., Hugelius, G., Jafarov, E., Krabbenhoft, D.P., Liu, L., Herman-Mercer, N., Mu, C., Roth, D.A., Schaefer, T., Striegl, R.G., Wickland, K.P., Zhang, T., 2018. Permafrost stores a globally significant amount of mercury. Geophys. Res. Lett. 45, 1463–1471. https://doi.org/10.1002/2017GL075571.
Schuster, P.F., Striegl, R.G., Aiken, G.R., Krabbenhoft, D.P., Dewild, J.F., Butler, K., Kamark, B., Dornblaser, M., 2011. Mercury export from the Yukon River Basin and potential response to a changing climate. Environ. Sci. Technol. 45, 9262–9267. https://doi.org/10.1021/es202068b.
Selin, N.E., 2009. Global biogeochemical cycling of mercury: a review. Annu. Rev. Environ. Resour. 34, 43–63. https://doi.org/10.1146/annurev.environ.051308.084314.
Sheng, J., Wang, X., Gong, P., Tian, L., Yao, T., 2012. Heavy metals of the Tibetan top soils: level, source, spatial distribution, temporal variation and risk assessment. Environ. Sci. Pollut. Res. 19, 3362–3370. https://doi.org/10.1007/s11356-012-0857-5.
Stein, E.D., Cohen, Y., Winer, A.M., 1996. Environmental distribution and transformation of mercury compounds. Crit. Rev. Environ. Sci. Technol. 26, 1–43. https://doi.org/10.1080/10643389609388485.
Sun, S., Kang, S., Huang, J., Chen, S., Zhang, Q., Guo, J., Liu, W., Neupane, B., Qin, D., 2017. Distribution and variation of mercury in frozen soils of a high-altitude permafrost region on the northeastern margin of the Tibetan Plateau. Environ. Sci. Pollut. Res. 24, 15078–15088. https://doi.org/10.1007/s11356-017-9088-0.
The Global Land One-kilometer Base Elevation (GLOBE) Digital Elevation Model, Version 1.0. National Oceanic and Atmospheric Administration, National Geophysical Data Center, 325 Broadway, Boulder, Colorado 80305-3328, U.S.A. Digital data base on the World Wide Web(URL: http://www.ngdc.noaa.gov/mgg/topo/globe.html) and CD-ROMs.
UNEP, 2013. The global mercury assessment 2013. Emiss. Releases Environ. Transp. 44. Glob. Mercur. Assess. 2013 sources.
Wang, B., French, H.M., 1995. Permafrost on the Tibet plateau, China. Quat. Sci. Rev. 14, 255–274. https://doi.org/10.1016/0277-3791(95)00006-B.
Wang, G., Li, Y., Wu, Q., Wang, Y., 2006. Impacts of permafrost changes on alpine ecosystem in Qinghai-Tibet Pwanglateau. Sci. China Earth Sci. 49, 1156–1169. https://doi.org/10.1007/s11430-006-1156-0.
Wang, L., Wang, S., Zhang, L., Wang, Y., Zhang, Y., Nielsen, C., McElroy, M.B., Hao, J., 2014. Source apportionment of atmospheric mercury pollution in China using the GEOS-Chem model. Environ. Pollut. 190, 166–175. https://doi.org/10.1016/j.envpol.2014.03.011.
Wang, X., Luo, J., Yin, R., Yuan, W., Lin, C.J., Sommar, J., Feng, X., Wang, H., Lin, C., 2017. Using mercury isotopes to understand mercury accumulation in the montane forest floor of the Eastern Tibetan Plateau. Environ. Sci. Technol. 51, 801–809. https://doi.org/10.1021/acs.est.6b03806.
Wang, X., Yang, H., Gong, P., Zhao, X., Wu, G., Turner, S., Yao, T., 2010. One century sedimentary records of polycyclic aromatic hydrocarbons, mercury and trace elements in the Qinghai Lake, Tibetan Plateau. Environ. Pollut. 158, 3065–3070. https://doi.org/10.1016/j.envpol.2010.06.034.
Wang, X., Yuan, W., Lin, C.J., Zhang, L., Zhang, H., Feng, X., 2019. Climate and vegetation as primary drivers for global mercury storage in surface soil. Environ. Sci. Technol. 53, 10665–10675. https://doi.org/10.1021/acs.est.9b02386.
Wu, Q., Zhang, T., 2010. Changes in Active Layer Thickness over the Qinghai - Tibetan Plateau from 1995 to 2007 115, pp. 1–12. https://doi.org/10.1029/2009JD012974.
Xue, W., Kwon, S.Y., Grasby, S.E., Sunderland, E.M., Pan, X., Sun, R., Zhou, T., Yan, H., Yin, R., 2019. Anthropogenic influences on mercury in Chinese soil and sediment revealed by relationships with total organic carbon. Environ. Pollut. 255, 113186. https://doi.org/10.1016/j.envpol.2019.113186.
Yang, Y., Ji, C., Chen, L., Ding, J., Cheng, X., Robinson, D., 2015. Edaphic rather than climatic controls over 13C enrichment between soil and vegetation in alpine grasslands on the Tibetan Plateau. Funct. Ecol. 29, 839–848. https://doi.org/10.1111/1365-2435.12393.
Yang, Y.K., Zhang, C., Shi, X.J., Lin, T., Wang, D.Y., 2007. Effect of organic matter and pH on mercury release from soils. J. Environ. Sci. 19, 1349–1354. https://doi.org/10.1016/S1001-0742(07)60220-4.
Yao, T., Thompson, L.G., Mosbrugger, V., Zhang, F., Ma, Y., Luo, T., Xu, B., Yang, X., Joswiak, D.R., Wang, W., Joswiak, M.E., Devkota, L.P., Tayal, S., Jilani, R., Fayziev, R., 2012. Third Pole environment (TPE). Environ. Dev. 3, 52–64. https://doi.org/10.1016/j.envdev.2012.04.002.
Zhang, H., Yin, R.S., Feng, X. Bin, Sommar, J., Anderson, C.W.N., Sapkota, A., Fu, X.W., Larssen, T., 2013. Atmospheric mercury inputs in montane soils increase with elevation: evidence from mercury isotope signatures. Sci. Rep. 3, 1–8. https://doi.org/10.1038/srep03322.
Zhang, Q., Huang, J., Wang, F., Mark, L., Xu, J., Armstrong, D., Li, C., Zhang, Y., Kang, S., 2012a. Mercury distribution and deposition in glacier snow over Western China. Environ. Sci. Technol. 46, 5404–5413. https://doi.org/10.1021/es300166x.
Zhang, Y., Jacob, D.J., Horowitz, H.M., Chen, L., Amos, H.M., Krabbenhoft, D.P., Slemr, F., St. Louis, V.L., Sunderland, E.M., 2016. Observed decrease in atmospheric mercury explained by global decline in anthropogenic emissions. Proc. Natl. Acad. Sci. U. S. A 113, 526–531. https://doi.org/10.1073/pnas.1516312113.
Zhang, Y., Jaeglé, L., Van Donkelaar, A., Martin, R.V., Holmes, C.D., Amos, H.M., Wang, Q., Talbot, R., Artz, R., Brooks, S., Luke, W., Holsen, T.M., Felton, D., Miller, E.K., Perry, K.D., Schmeltz, D., Steffen, A., Tordon, R., Weiss-Penzias, P., Zsolway, R., 2012b. Nested-grid simulation of mercury over North America. Atmos. Chem. Phys. 12, 6095–6111. https://doi.org/10.5194/acp-12-6095-2012.
Zhou, Y., Aamir, M., Liu, K., Yang, F., Liu, W., 2018. Status of mercury accumulation in agricultural soil across China: spatial distribution, temporal trend, influencing factor and risk assessment. Environ. Pollut. 240, 116–124. https://doi.org/10.1016/j.envpol.2018.03.086.
Zhu, Y., Zhang, Y., Liu, M., Chen, L., He, Q., Ye, Z., Sun, J., 2014. Distribution and pollution assessment of the mercury in soils of Tibet. Ecol. Environ. Sci. 23, 1487–1491. https://doi.org/10.16258/j.cnki.1674-5906.2014.09.016 (in Chinese).